Seismic and well log characterization of fractures for geothermal exploration in hard rocks

Mattia Aleardi,[1] Alfredo Mazzotti,[1] Andrea Tognarelli,[1] Simonetta Ciuffi[2] and Michele Casini[2]

[1]*Earth Sciences Department, University of Pisa, Via S. Maria 53, I-56126 Pisa, Italy. E-mail: mattia.aleardi@dst.unipi.it*
[2]*Enel Green Power, Via Andrea Pisano 120, I-56122 Pisa, Italy*

SUMMARY

We study the well log and seismic responses of intensively fractured portions of deep intrusive/metamorphic rocks in southern Tuscany (Italy), which constitute the main drilling targets of the geothermal exploration in the Larderello–Travale area. In particular, the target we consider is located near the contact between a deep Pliocene granitic intrusion and the overlying Palaeozoic metamorphic basement. Sonic, density and borehole image logs are analysed together with post-stack reflection attributes and reflection amplitude versus source to receiver azimuth (AVAZ) responses. It turns out that the intense fracturing in the contact zone causes significant decreases in the density and *P*-wave velocity, and that fracture planes exhibit very high dips and a common preferential direction. The fractured zone found by the well coincides with peculiar alignments of high-amplitude signals in the 3-D seismic stack volume, which are particularly visible on the reflection strength and instantaneous phase time slices. The normal incidence synthetic seismogram based on the log data matches the observed stack trace nearest to the well and confirms that the high-amplitude reflection occurs at the fractured zone. We then consider the pre-stack domain to study the same reflections on bin gathers that are close to the well and coincident with the anomalies in the 3-D volume. In particular, we perform AVAZ analysis to detect possible anisotropic features in the reflected amplitudes due to the preferential orientation of the fractures, and we study the effect of crack density on the seismic responses and on velocity and density values. To this end, we build simplified models where a level with vertical fractures is encased in tight isotropic rocks. Notwithstanding the suboptimal quality of the seismic data, we estimate the overall matching between the borehole information and the seismic response as fair. In particular, the azimuthal amplitude variation of the reflections from the studied fractured zone has a sinusoidal trend that is quite consistent with the fracture planes' orientation as indicated by the image logs. Moreover, the comparison between the actual AVAZ response and the AVAZ responses of synthetic seismograms generated on models with different crack densities suggests that it may be feasible to estimate crack density values from the azimuthal amplitude variation of the observed reflections, within the resolution of the seismic data.

Key words: Controlled source seismology; Seismic anisotropy; Fractures and faults.

1 INTRODUCTION

The drilling of geothermal wells at the Larderello field in southern Tuscany (Italy) started approximately 100 yr ago to exploit a shallow carbonate reservoir, which was found at less than 1000 m depth and has temperatures of approximately 250 °C. Since the 1980s, the targets of geothermal exploration have been at 3000–4000 m below sea level, where the first deep wells encountered a 300–350 °C superheated steam reservoir (Barelli *et al.* 1995, 2000). This reservoir is mainly hosted in the metamorphic basement and underlying granite and, unlike the shallow reservoir, has a rather inhomogeneous permeability. Casini *et al.* (2010) showed that a correlation exists between a high-amplitude reflector that is visible in the stack volume and the fractures located near the contact separating the underlying Pliocene granite and the overlying basement. It is this fractured zone that we aim at characterizing in this work.

As demonstrated by several authors (Lamarche 1992; Nakagome *et al.* 1998; Matsushima *et al.* 2003; Casini *et al.* 2010; Kent

et al. 2013; Lüschen *et al.* 2014; Pussak *et al.* 2014; Giustiniani *et al.* 2015), reflection seismic methods yield valuable results for geothermal exploration in both clastic/carbonatic rocks and volcanic/metamorphic rocks. Thus, we make use of 3-D seismic data and information from a deep well to assess whether the fractured zone we consider yields discernible signatures in the seismic data. We consider both post-stack seismic images and pre-stack amplitude-versus-azimuth (AVAZ) analysis. The latter seismic method has gained popularity for investigating fractured reservoirs. In fact, aligned fractures can influence the propagation velocity of seismic waves in the Earth. For vertically aligned fractures, such as those assumed in this study, the fractured rock can be described as a transverse isotropic medium with a horizontal axis of symmetry (HTI medium). In an HTI medium, the amplitude of the seismic reflections varies not only with the incident angle (as in the conventional amplitude-versus-angle—AVA analysis) but also with the source to receiver azimuth and can be expressed in terms of the azimuth, incident angle and three anisotropic parameters (Thomsen 1986) that characterize the fractured medium. Assuming a single reflecting interface that separates an isotropic half-space over a transverse isotropic medium, Ruger (1997) derived a simplified equation that models the AVA variations of the reflection coefficients for different source–receiver azimuths. The Ruger equation (or other suitable equations) and ray tracing algorithms enable the computation of synthetic convolutional seismograms for varying source to receiver distances and source to receiver azimuths.

In the 1990s, Lynn *et al.* (1996) and Mallick *et al.* (1998) demonstrated that measurable differences exist in the seismic AVA responses parallel and perpendicular to fractures, suggesting that AVAZ would be a viable technology. Therefore, AVAZ analysis began to be used on 3-D data sets, quickly providing evidence of its importance (Gray *et al.* 1999; Vetri *et al.* 2003). However, to our knowledge, AVAZ techniques have not been extensively applied to characterize the seismic response of metamorphic/intrusive rocks, such as those that form the deepest levels of the Larderello–Travale geothermal reservoir, which motivates this study.

In the following sections, we start with a brief description of the geology of the Larderello–Travale area and with a summary of the acquisition and processing of the 3-D seismic data. These two sections derive from previous publications (e.g. Casini *et al.* 2010) and serve to introduce the reader to the local geological setting and the main characteristics of the 3-D seismic survey. Then, we describe the post-stack analysis and the log data of the deep well, in particular, the density and velocity changes in the considered fractured zone. To link the model data, that is the *P*-wave velocity and density contrasts given by the bore-hole logs, to the observed seismic data, we compute the normal incidence synthetic seismogram and check the correspondence with the actual seismic stack trace located near the well. The next section illustrates the pre-stack AVAZ analysis. We start by describing the fractured zone as it results from a full waveform sonic (FWS) recording and from a circumferential bore-hole imager log (CBIL), from which we extract information about the main orientation of the fractures. Based on the well data and statistical techniques, we develop several models that keep the encasing media and the strike of the fractures within the target interval constant but change the crack density (fracture density per volume; see, e.g. Krasovec *et al.* 1998) in the target zone from 0 (no fractures) to 0.1. We then check the matching between the simulated velocities and density with the actual velocity and density logs in the fractured interval, as well as the matching between the AVAZ of

the synthetic seismograms and the AVAZ of the actual reflections. The final section highlights the limitations and assumptions of our study and discusses the possible outcomes that 3-D seismic studies can provide in this geothermal area or in other areas with similar characteristics.

2 GEOLOGICAL SETTING OF THE LARDERELLO TRAVALE GEOTHERMAL FIELD

Geothermal systems often occur in continental extensional tectonic environments characterized by high heat flow (Barbier 2002; Batini *et al.* 2003). Extension also characterizes southern Tuscany, where the most important geothermal fields of Italy are located (Fig. 1). Larderello–Travale is one of these fields, and its geological structure is the consequence of two contrasting processes. The first process is the convergence and subsequent collision between the European and African margins (Late Cretaceous–Early Miocene) (Boccaletti *et al.* 1980). The second process is related to the extensional tectonic deformation that has affected the inner part of the Northern Apennines since the Miocene (Carmignani & Kligfield 1990; Jolivet *et al.* 1990; Bertini *et al.* 1991; Baldi *et al.* 1994; Carmignani *et al.* 1994, 1995; Jolivet *et al.* 1998). Extensional tectonics are accompanied by the emplacement of granites originating from the mixing of crustal and mantle magmas. Therefore, southern Tuscany is presently characterized by high heat flow (120 mW m^{-2} on average), with local peaks of up to 1000 mW m^{-2} (Batini *et al.* 2003; Bertini *et al.* 2006). The seismic and well data considered in this study are located in the Travale area in the ESE part of the Larderello–Travale geothermal system (Fig. 1).

The lithostratigraphic column of the Travale area is composed of the following (from top to bottom):

(1) Neogene marine and continental sediments.
(2) Ligurian Unit—flysch facies formation, mainly shales (Lower Cretaceous–Eocene).
(3) Tuscan Nappe—sandstones and limestones (Upper Triassic–Lower Miocene).
(4) Tectonic Wedge–anhydrites, quartzites and phyllites (Lower Permian–Upper Triassic).
(5) Metamorphic basement—phyllites and mica schists (Lower Palaeozoic).
(6) Contact-metamorphic rocks (skarns and hornfels).
(7) Granitic intrusions (Pliocene).

As discussed in Bertini *et al.* (2005), two different reservoirs were identified:

(1) A shallow, steam-dominated reservoir of medium to high permeability in carbonate rocks. This reservoir is characterized by temperatures between 220 and 250 °C and pressures of approximately 3–4 MPa.
(2) A superheated steam reservoir localized in the metamorphic basement and in the granitic intrusion with temperatures between 300 and 350 °C and pressures of approximately 5–7 MPa.

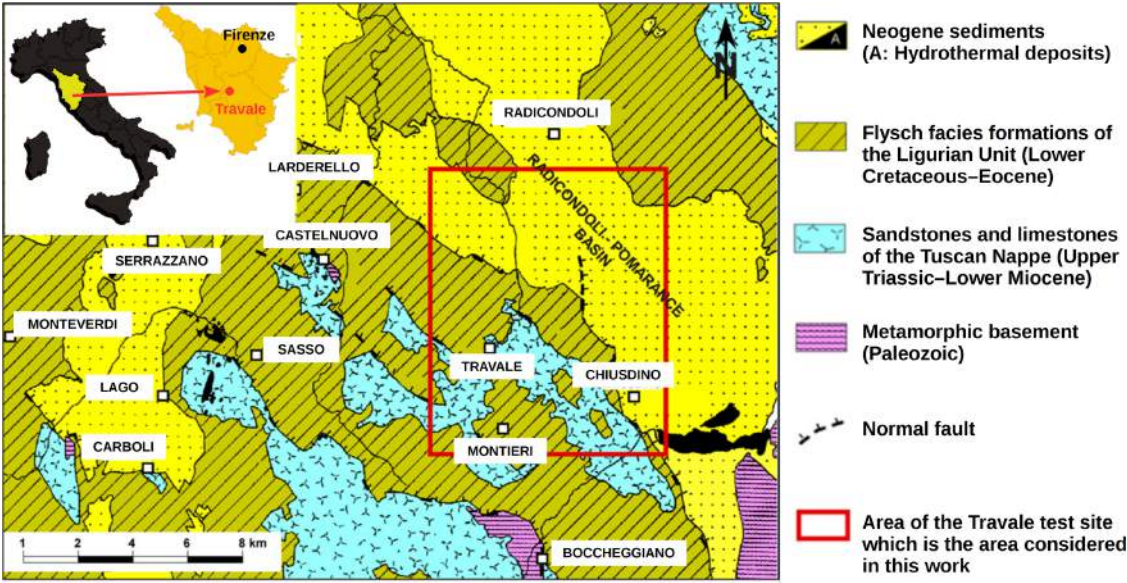The fractures located in this deeper reservoir are the fractures that we consider in this study.

Figure 1. Location of the Travale test site and schematic geological map of the Larderello–Travale area (modified from Casini *et al.* 2010).
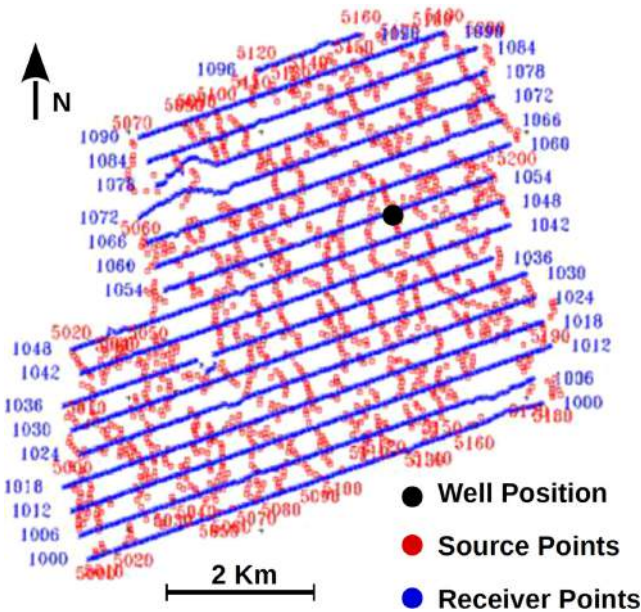

Figure 2. Actual acquisition layout of the 3-D seismic survey at the Travale site. The black dot indicates the position of the well considered in this work. Blue dots and red dots represent receiver and source positions, respectively.

Table 1. Acquisition parameters.

Parameter	Characteristic
Energy source	Dynamite
Source pattern	Single hole
Dynamite charge	1–5 kg
Shot-hole depth	12 m
Shot-hole spacing	80 m
Receiver spacing	50 m
Active channels	720
Source line interval	500 m
Receiver line interval	480 m
Sampling rate	2 ms
Recording time	8 s
Total number of shots	1484
Total number of recorded traces	801140

3 A BRIEF OUTLINE OF THE 3-D SEISMIC DATA ACQUISITION AND PROCESSING

The 3-D seismic survey was conducted in 2003 with a bin size of 25 m × 40 m and with explosives as the energy source. The actual acquisition layout was based on a standard orthogonal geometry with a recording spread of 720 active stations and source to receiver offsets ranging from 50 m to 3800 m (Fig. 2). The acquisition parameters (Table 1) determined a minimum fold over the subsurface target area of 16, with an irregular source to receiver azimuth and source to receiver offset distributions (Fig. 3) due to both the known limitations of the orthogonal acquisition geometry and the many accessibility problems (especially for the source loca-

tions, as shown in Fig. 2). The irregularity is prominent for source to receiver offsets greater than 1500 m (Fig. 3), with significant differences in the azimuthal coverage (as large as 500 units for offsets up to 4000 m). This fact indicates that, on average, the greater the source to receiver offset is, the worse the azimuthal coverage of the traces becomes. For single bin gathers or for groups of adjacent bin gathers, this undesirable condition may significantly worsen due to local accessibility limitations in the acquisition. We will come back to this issue when we discuss the results of the AVAZ analysis. The ensemble of accessibility problems, ground roll noise contamination and rough topography resulted in data quality that was quite variable from place to place and required significant processing effort. Details on the applied processing sequence can be found in Casini *et al.* (2010) and thus only a brief summary is given here.

The aim of the processing was twofold (the main processing steps are listed in Table 2). On one hand, we had to improve the signal-to-noise ratio (S/N) and the coherency of the reflected signals. Steps 2, 3, 4, 5, 8, 11 and 13, which were performed before the stacking operation and step 18, which was performed after stacking, were specifically devoted to this goal. On the other hand, we had to pay particular attention to preserve the signal amplitudes because we wanted to use the amplitudes of the reflections as diagnostic indicators, either in the pre-stack domain or in the post-stack domain.
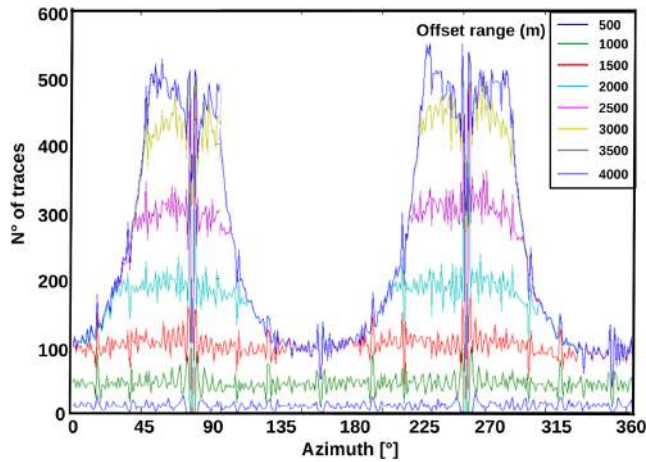
Figure 3. Offset-azimuth distribution for the whole 3-D seismic data. The colored lines indicate different offset ranges as indicated in the labels. Note the very irregular offset-azimuth distribution, with a distinct polarization at approximately 60–70 deg N (±180 deg) that approximately corresponds to the orientation of the receiver lines (see Fig. 2).

Table 2. Main processing steps sequentially listed. Steps 15 and 16 are applied to perform AVAZ analyses.

Step	Description
1	Geometry assignment and bad trace removal
2	Statistical despiking
3	Bandpass filter (4–8–70–80 Hz)
4	Ground-roll attenuation with time-offset variant filter
5	Refraction statics
6	Geometrical spreading amplitude recovery
7	Surface-consistent amplitude compensation
8	FX deconvolution in common shot domain
9	Surface consistent predictive deconvolution
10	Velocity analysis
11	Surface-consistent residual statics
12	Refinement of velocity field
13	Bin consistent residual statics
14	Normal moveout (NMO)
15	Incident angle gathering
16	Source–receiver azimuth binning for AVAZ analysis
17	Stack
18	FXY deconvolution
19	Post-stack Kirchoff time migration

Steps 6, 7 and 9 in Table 2 were specifically devoted to this task. All the other steps were required to form the 3-D seismic image that was needed to conduct the structural interpretation of the area. Note that only a single multichannel filtering operation (step 8 in Table 2) was applied to enhance the lateral continuity of the data and no gain functions or other data independent algorithms that could potentially distort the amplitude responses of the reflections were applied. A detail of the final 3-D seismic volume is shown in Fig. 4. Highlighted is the top of the Pliocene granite that was interpreted based on well log data, such as the gamma-ray log that shows a sudden increase of gamma radiation passing from the overlying Palaeozoic metamorphic basement to the granitic intrusion. Although the processing sequence improved the data quality and preserved the amplitudes of the signal, the low S/N ratio of the final data and the anomalies in the distributions of source to receiver offsets and source to receiver azimuths made AVAZ analysis particularly problematic if performed on single gathers; thus, trace averaging was needed to increase the data quality.

4 SEISMIC AND WELL LOG CHARACTERIZATION OF THE TARGET FRACTURED ZONE: POST-STACK ANALYSIS

We focus our attention on a depth segment of the deep well (indicated in Fig. 4) that reached a structural high of the granites and extensively logged the considered fractured zone (Fig. 5). The sharp density decreases in the density log (Fig. 5a) help to locate several fractures, some of which are indicated by arrows. In particular, the green arrow indicates the target fracture zone that is also investigated by the CBIL shown in Fig. 9. The decreases in density and *P*-wave velocity (Figs 5a and b, respectively) associated with the presence of fractures cause strong reflection coefficients and complex interferences among the reflected wavelets.

To link the model data, that is the sequence of density and velocity contrasts given by the bore-hole logs, to the observed seismic data of the 3-D volume, we compare the normal incidence synthetic seismogram with the stack trace nearest to the considered well (Fig. 5e). To compute the synthetic seismogram, we simply convolve the normal incidence reflection coefficients (Fig. 5d) with a Ricker wavelet with the same dominant frequency (30 Hz) as the observed stack traces. The resulting synthetic seismogram (Fig. 5e, black trace) adequately matches the observed stack trace (Fig. 5e, blue trace) as they both show concordant high-amplitude reflections at approximately 0.85 s, which is the two-way time that corresponds to the fractured level target of our study. Extending our observations to the 3-D volume near the well, the fractured zone produces a high-amplitude reflector characterized by good lateral continuity (Fig. 6).

To verify whether we might extract additional indicators to characterize the fractures, we extract several complex attributes (Taner *et al.* 1979; Robertson & Fisher 1988; Taner 2001) from the seismic traces, namely reflection strength, instantaneous phase, instantaneous frequency and other frequency-derived attributes such as sweetness, instantaneous bandwidth and instantaneous frequency at the envelope peaks. The time slices at 0.85 s of the reflection strength and of the instantaneous phase (Figs 7 and 8, respectively) show an elongated zone with high-reflection strength and continuous phases that corresponds to the target fractured level at the well location. These high values of the reflection strength are consistent with the contrasts in *P*-wave velocity and density associated with the presence of fractures. The alignment of the instantaneous phase attribute (Fig. 8) coincides with and extends the anomaly observed in the reflection strength. The lateral continuity of the instantaneous phase and the high-reflection strength are interpreted as features of the lateral extension of the fractured zone and will direct our further analyses in the pre-stack seismic data. Conversely, the other attributes associated with the frequency of the signal, which we had hoped could evidence features related to the presence of fractures (e.g. absorption phenomena), did not contribute to pinpoint any particular anomaly and are therefore not discussed here.

5 SEISMIC AND WELL LOG CHARACTERIZATION OF THE TARGET FRACTURED ZONE: MODELLING AND AVAZ ANALYSIS

Our attempt at evaluating the azimuthal variations of the reflected amplitudes at given incident angles aims at identifying anisotropy possibly related to the presence of spatially aligned fractures. In fact, the FWS log and the CBIL that were recorded at the depths of the
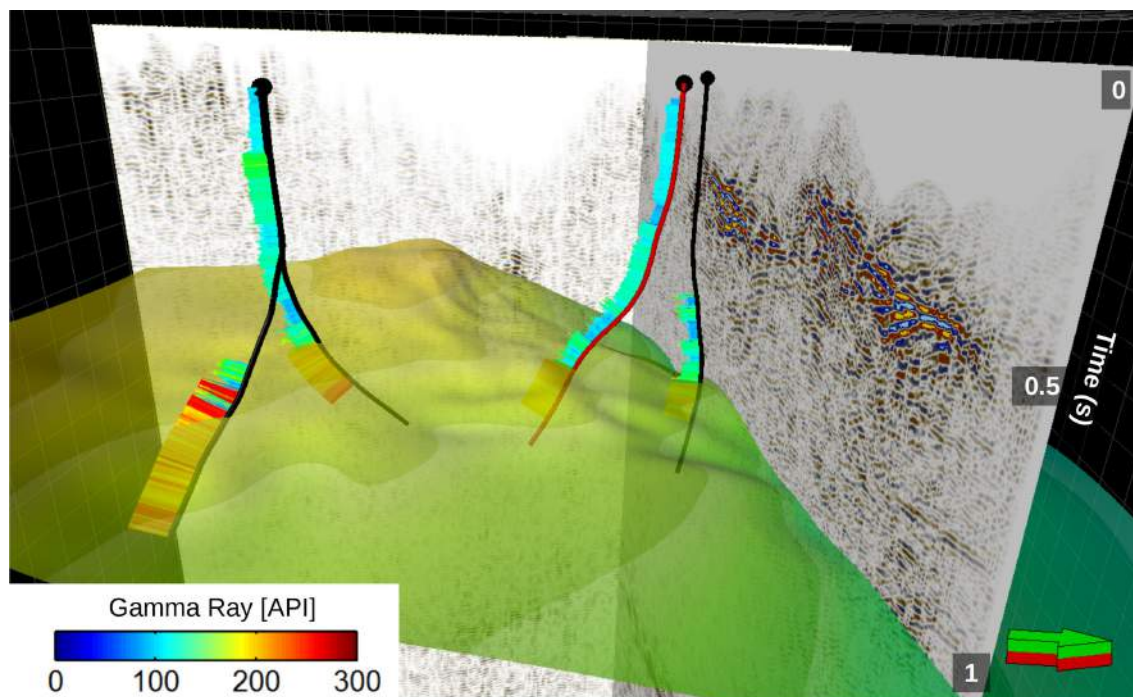
Figure 4. Close-up of the 3-D seismic volume in the Travale area. The smooth surface represents the interpreted top of the Pliocene granites. Several well trajectories are represented together with the recorded gamma-ray log. The red path indicates the trajectory of the well whose data are used throughout this work, whereas the arrow in the bottom right indicates the geographic north. Note that an increase in gamma-ray radiation occurs when passing from the overlying metamorphic rock to the deeper granites.
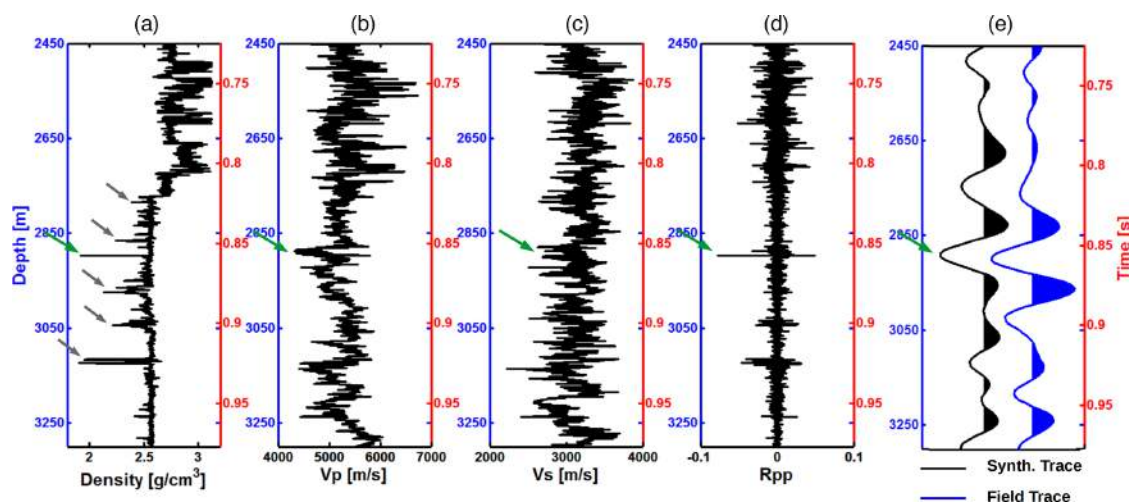

Figure 5. (a) Density, (b) *P*-wave velocity, (c) *S*-wave velocity logs, (d) *P*-wave normal incidence reflection coefficients and (e) synthetic seismogram and actual stack trace in the depth/time segment that includes the fractured zone considered in this study. Depth-to-time conversion was performed by using check shot recordings, and the resulting two-way timescale is represented on the vertical axes on the right of the frames. The arrows indicate sharp density decreases that are associated with the occurrence of fractures. The green arrow indicates the position of the fractured zone of interest.

considered fractured interval indicated the presence and orientation of several fractures. Therefore, we describe the effects that oriented fracture sets have on the velocities and density of the fractured medium and on the azimuthal response of reflected *P* waves.

From approximately 2875 m to 2950 m depth, the recorded waveforms and their representation in instantaneous amplitude (Fig. 9a) show strong attenuation of the wave phases (enclosed in the rectangular area of Fig. 9a), particularly of Stoneley waves (Tang *et al.* 1991; Bakku *et al.* 2012) and delays of direct *P*- and *S*-wave arrivals. The CBIL image, shown in Fig. 9(b), is pertinent to a segment where the attenuation of the waveforms is particularly severe and, together

with other image logs (e.g. resistivity micro scanner), were analysed in detail to identify natural fractures and fractures induced by drilling. The natural fractures are observed as sinusoidal dark lineaments around 360 deg in the CBIL images, with the closed fractures better evidenced by the amplitude image while the open fractures are evidenced by both the amplitude and the traveltime images. The integrated interpretation of the CBIL data and the other available logs enabled the identification of the open or closed nature of the fractures, as indicated by the arrows in Fig. 9(b). Note that the open fractures are concentrated at a depth of 2900 m, while the closed fractures are dispersed along the entire depth segment. This
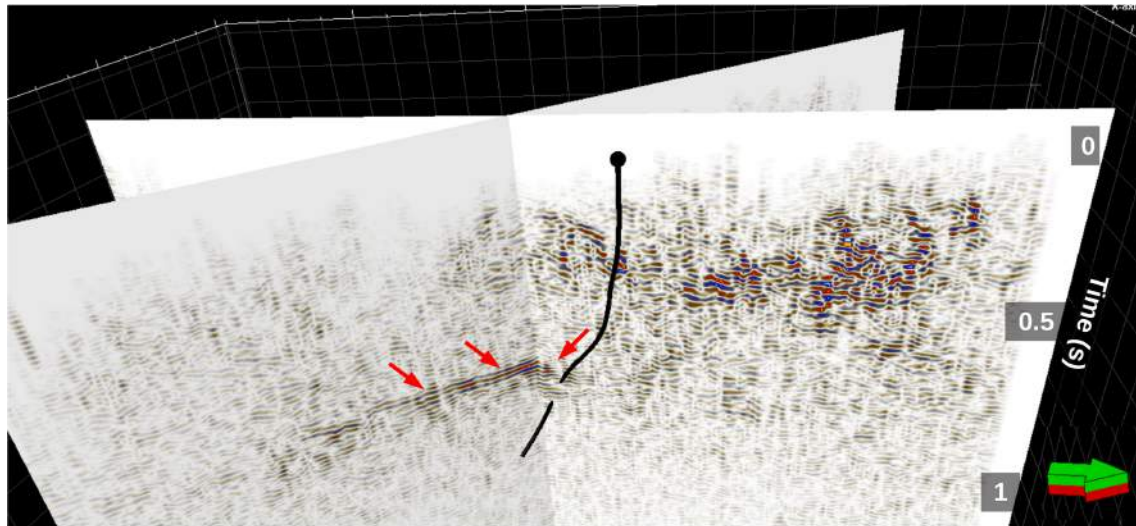
Figure 6. Close-up of two lines extracted from the 3-D volume that intersect near the well location. The arrow on the bottom right corner indicates the geographic north. Note the high-amplitude reflector produced by the fractured zone and highlighted by the red arrows.
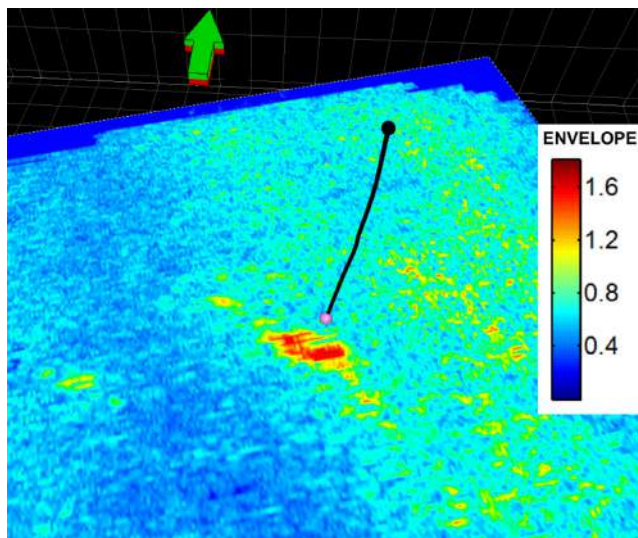

Figure 7. Time slice at 0.85 s of the 3-D seismic volume representing the reflection strength attribute. The area with high-reflection strength intersected by the well corresponds to the fractured zone studied in this work. The black line indicates the well path and the arrow at the top of the figure points to the geographic north.
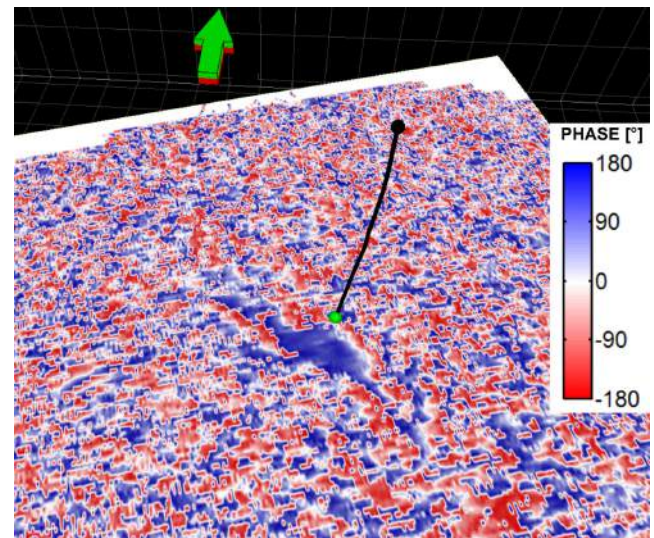

Figure 8. Time slice at 0.85 s of the 3-D seismic volume representing the instantaneous phase. Note the peculiar alignment of the instantaneous phase, which matches the location of the high-reflection strength shown in Fig. 7. The black line indicates the well path and the arrow at the top of the figure points to the geographic north.

peculiarity has a direct consequence on the density and velocity logs, in the sense that open fractures cause sharp density decreases while closed fractures produce less prominent (even negligible) effects on the density. At the same time, velocities sense both open and closed fractures. This different behaviour and the different resolution of the two logging tools explain the different responses of the density and sonic logs (Figs 5a and b): the *P*-wave velocity shows a decrease along the entire fractured interval (approximately 20 m in Fig. 5b), while the density shows a spiky decrease at the depth of the open fractures.

All the fractures in the considered interval show a NNW-SSE oriented strike (140–160 deg N clockwise) and very high dips ranging between 70 and 83 deg (Fig. 9c). The fracture attitude, as reconstructed by this CBIL, is similar to the information recovered from other CBIL images (not shown here) that were recorded in different depth intervals along the metamorphic basement and the granitic

intrusion. Therefore, the CBIL study reveals a fracture model characterized by lineaments that strike NNW-SSE, with very high dips, and an average ENE plunge. These characteristics are also consistent with the main structural trend of the study area (Bertini *et al.* 2006) and with the spatial orientation of the elongated alignment evidenced by the reflection strength and instantaneous phase attributes (Figs 7 and 8).

The organized nature of the fractures, with a general common orientation and near vertical dip as shown by the CBIL, led us to approximate the fractured zone as an anisotropic medium, in particular as a transverse isotropic medium with a horizontal symmetry axis (HTI medium). As observed by several authors (Lynn *et al.* 1996; Adriansyah & McMechan 2001; Shen *et al.* 2002), the reflections from the top of an HTI medium, such as fractured limestones, show an azimuthal dependence of the reflected amplitudes; hence their amplitudes vary not only with the incidence angle but also as
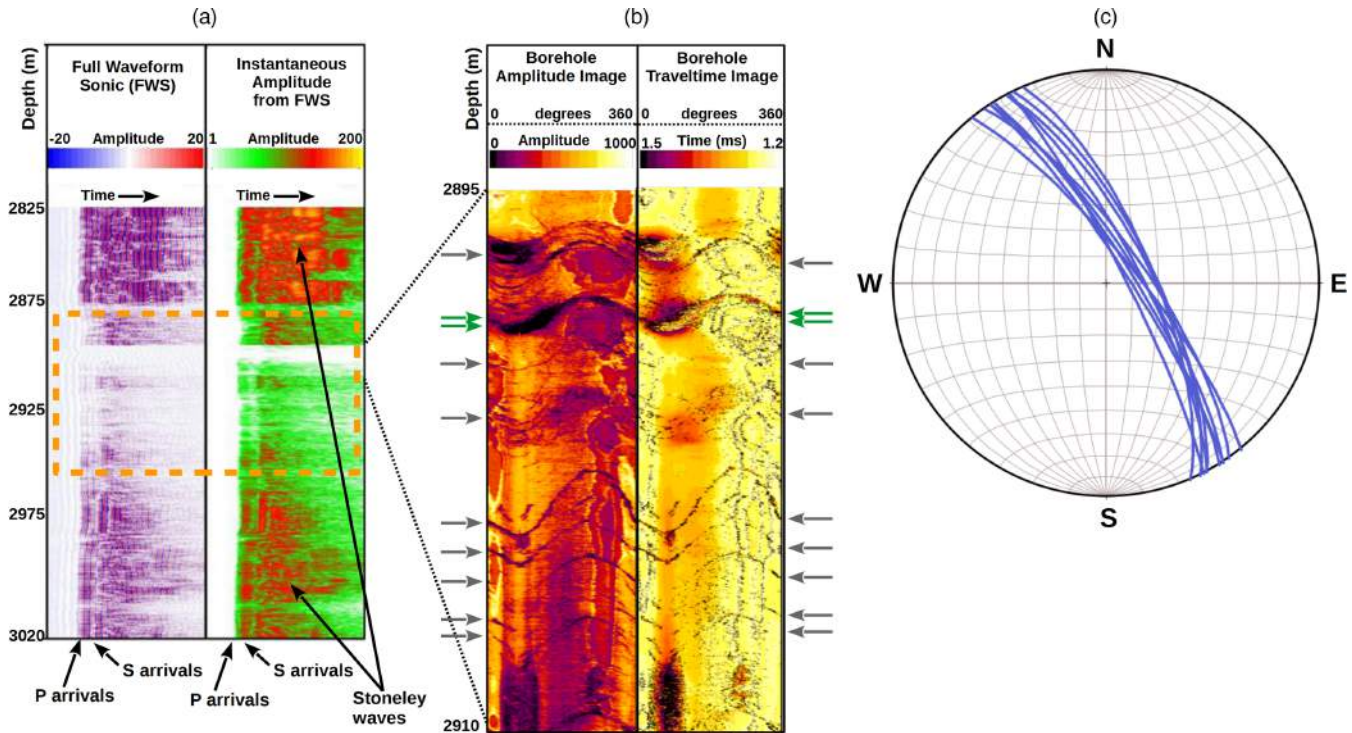
Figure 9. (a) Full waveform sonic (FWS) log and its instantaneous amplitude representation. (b) Circumferential borehole imager log (CBIL). (c) Schmidt plot depicting the dip and strike of the fractures in the depth interval 2895–2910 m. The rectangular area in (a) encloses a portion of the FWS data where the attenuation of Stoneley waves takes place. The CBIL shown in (b) includes both the amplitude image (on the left) and the traveltime image (on the right). The green arrows point to two closely spaced open fractures that are the likely cause of the sharp density decrease at 2900 m observed in the density log of Fig. 5(a). The other arrows indicate fractures that are interpreted as closed or filled fractures. Note that the Schmidt plot in (c) shows fractures with very similar strike and dip.

a function of the source to receiver azimuth. This peculiar feature is a direct consequence of the azimuthal variation of the reflection coefficient for *P* waves reflected from an HTI medium.

To check whether the observed AVAZ response is consistent with the model derived from the bore-hole data and to study the effect of crack density on the observed seismic response, we built five models with varying crack density in the fractured level and computed the synthetic responses (velocities, density and corresponding synthetic seismograms) to be compared with the actual responses. To build the models we considered an HTI fractured layer hosted in isotropic tight rocks. As indicated by the well information, the fractured rock has the same lithological composition as the encasing isotropic rocks and, we assumed, the same vertical variability in its elastic properties (i.e. in its velocities and density). Therefore, the elastic properties of the HTI medium and their statistical characteristics (vertical variability, covariance and mean value) can be computed by taking the elastic properties of the encasing isotropic rock and imposing different crack densities to mimic the presence of fractures. Appendix A describes the steps of the model building procedure. We calculated the elasticity tensor for each simulated crack density (Schoenberg & Sayers 1995; Krasovec *et al.* 1998), from which we derived the velocities of the equivalent effective HTI medium and the Thomsen's parameters γ, ε and δ (Thomsen 1986). Appendix B summarizes the relevant theoretical aspects. The densities were simply computed as weighted averages of the isotropic rock density and the fracture volume density, assuming vapor as the saturating fluid. For the special case of a crack density equal to zero, the target zone becomes a perfectly isotropic rock with the same properties as the encasing tight rocks. Therefore, all the models share the overburden, the encasing rocks and the strike of the

fractures and differ in the crack density of the fractured level from 2895 m to 2910 m depth, which is the interval where the FWS log registers strong attenuation in the wave phases and where the CBIL image shows several high-dip fractures (Fig. 9).

For each fractured model, we computed synthetic seismograms with varying source to receiver offsets and source to receiver azimuths, reproducing the configuration of the actual data as much as possible. To this end, the velocities and density logs of the various models were first upscaled to the dominant seismic wavelength by using the Backus averaging method (Backus 1962), and the *P*-wave reflection coefficients were computed for each resulting interface via the Ruger (1997) expression (see Appendix B). Note that the source to receiver azimuth in Appendix B is defined with respect to the symmetry-axis plane, which is perpendicular to the fracture plane. However, to facilitate the comparison between the synthetic and actual AVAZ, all the azimuths are referred to the geographic north.

5.1 Comparison between modelled and observed responses

The results of the simulations are illustrated in Figs 10–13 for fracture models with crack densities of 0, 0.025, 0.075 and 0.1, respectively. The simulated logs (red curves), the observed logs (blue curves) and the resulting synthetic seismograms for two azimuthal directions (60 and 150 deg) are shown. Two-way times are represented in the vertical axis and the target fractured level corresponds to a time position between 0.852 and 0.857 s. Note that the statistical approach we used to build the models enables to reproduce the variability of the observed logs in the fractured interval.
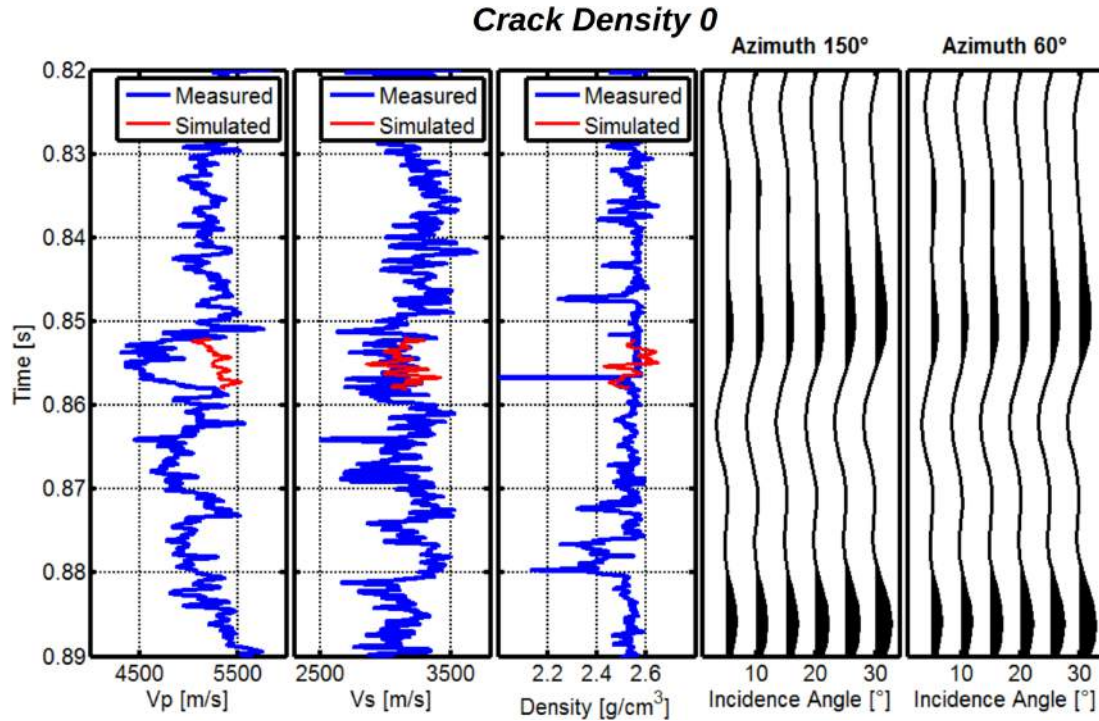
Figure 10. Modelling of fractures in the target interval between 0.852 and 0.857 s. The assumed crack density for the HTI medium is equal to 0, which is a perfectly isotropic medium. Therefore, in this case, the target zone has the same average properties of the tight encasing rocks. The *P*-wave velocity, *S*-wave velocity, density and two synthetic seismograms at different azimuths (150 and 60 deg) are plotted from left to right. The blue lines show the actual log data, whereas the simulated properties are in red. In this case, the simulated properties align with the measured properties in the un-fractured encasing rocks, and the two seismograms are identical.
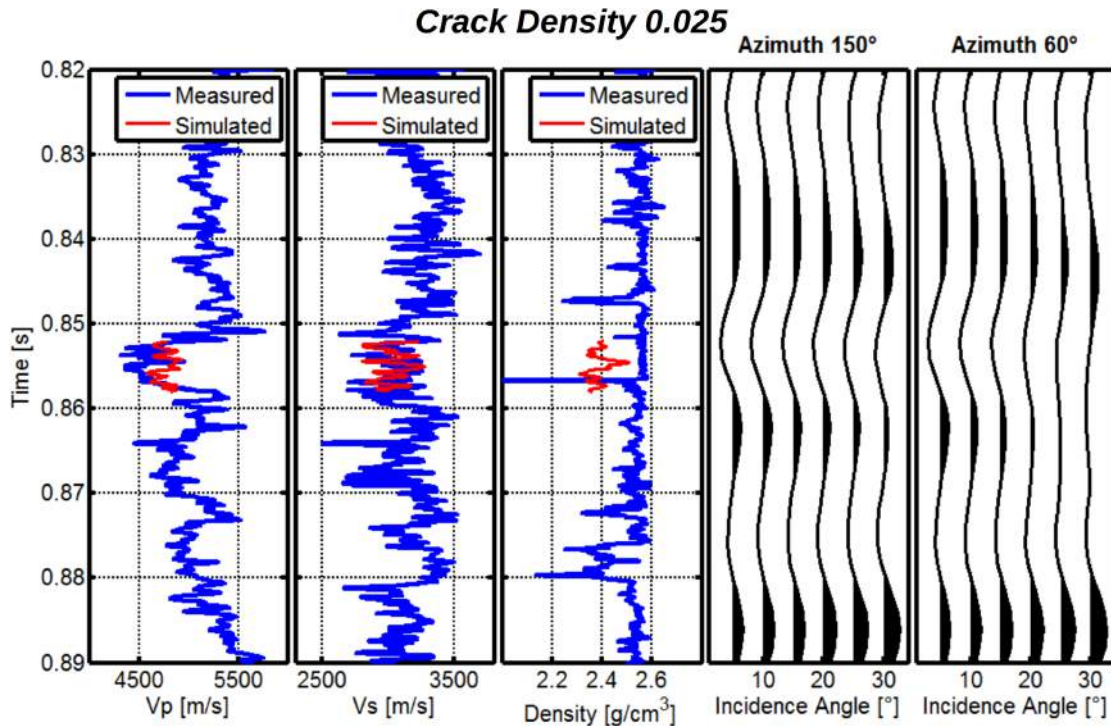

Figure 11. Same as Fig. 10 but for a crack density of 0.025, that is, we start simulating the presence of fractures and thus the average properties of the target zone differ from those of the tight encasing rocks. The *P*-wave velocity, *S*-wave velocity, density and two synthetic seismograms at different azimuths (150 and 60 deg) are plotted from left to right. The blue lines show the actual log data, whereas the simulated properties are in red. The simulated properties, particularly the *P*-wave velocity and density, show a significant decrease and the two seismograms at orthogonal azimuths exhibit differences.
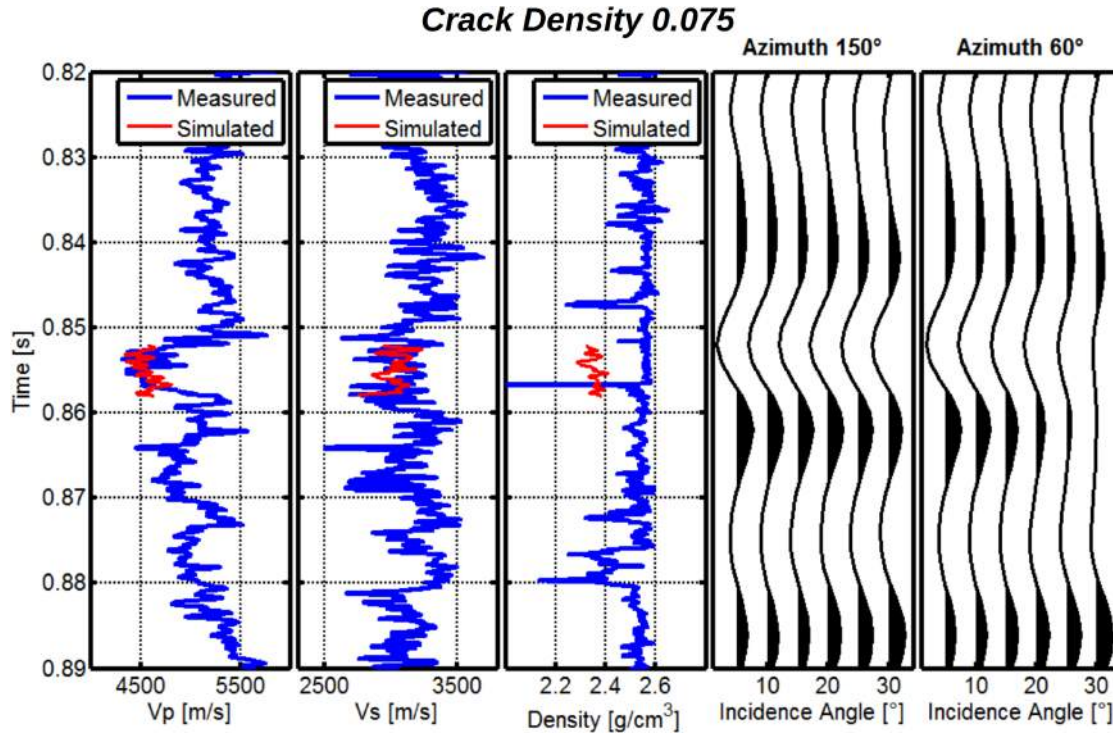
Figure 12. Same as Fig. 10 but for a crack density of 0.075. The *P*-wave velocity, *S*-wave velocity, density and two synthetic seismograms at different azimuths (150 and 60 deg) are plotted from left to right. The blue lines show the actual log data, whereas the simulated properties are in red. The simulated properties, particularly the *P*-wave and *S*-wave velocities, match the observed logs. The exception we observe for the density is discussed in the text. Note also the significant differences with azimuth of the reflections from the target zone shown by two seismograms at orthogonal azimuths.
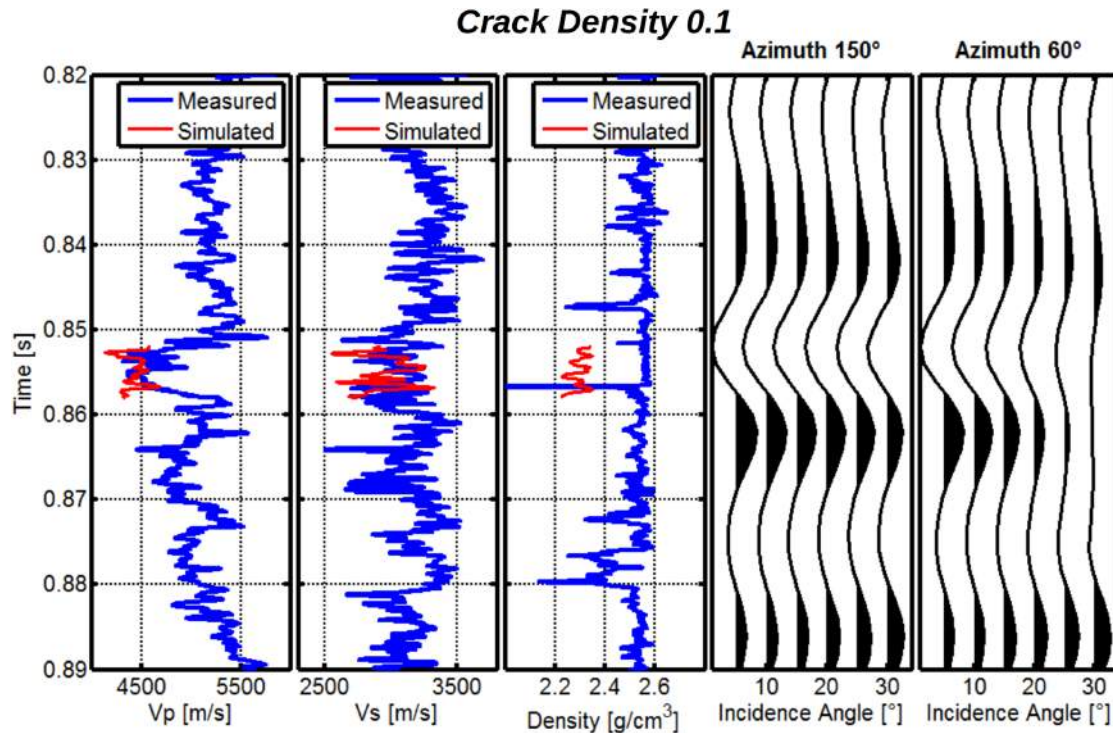

Figure 13. Same as Fig. 10 but for a crack density of 0.1. The *P*-wave velocity, *S*-wave velocity, density and two synthetic seismograms at different azimuths (150 and 60 deg) are plotted from left to right. The blue lines show the actual log data, whereas the simulated properties are in red. The simulated *P*-wave and *S*-wave velocities are now slightly lower than those measured. The differences between the two seismograms at orthogonal azimuths have further increased from the previous figure.

In the time interval pertaining to the fractured zone, the recorded logs (blue curves) show a strong decrease of *P*-wave velocity, a minor decrease of the *S*-wave velocity and a sharp, localized decrease of the density. Assuming a crack density equal to zero (Fig. 10), the simulated properties (red curves) are vertically aligned with the measured properties in the encasing isotropic rocks and differ markedly from the measured properties. Increasing the crack density (Figs 11–13) progressively decreases the *P*-wave velocity and density and slightly decreases the *S*-wave velocity. A good match between the observed and simulated *P*-wave and *S*-wave velocities of the fractured zone is reached for a crack density of 0.075 (Fig. 12).

The mismatch between the modelled density and the actual density occurs because the method used to build our models assumes homogeneously distributed open fractures, or more exactly, homogeneously distributed open ellipsoidal cracks. Therefore, the density we modelled can be thought of as an average bulk density over the entire interval. Instead, in our case, the considered fractured interval includes both open and closed fractures, with the open fractures concentrated at approximately 2900 m, which produces the spiky density decreases observed in the density log.

The synthetic seismograms computed for an incidence angle range from 5 to 30 deg at two different source–receiver azimuths (150 and 60 deg) are also represented in Figs 10–13. The azimuthal directions of 150 and 60 deg correspond, respectively, to the directions of waves propagating parallel and perpendicularly to the fracture strike, as determined by the CBIL analysis (Fig. 9c). Focusing on the reflections generated by the fractured HTI medium (located between 0.85 and 0.86 s), we note that for the isotropic model with no fractures (Fig. 10), reflections from the target level are hardly visible and the seismograms pertinent to the two azimuths are identical. Increasing the crack density of the fractured zone (Figs 11–13) creates increasingly energetic reflections with progressively prominent azimuthal variations.

To examine the effect of crack density on azimuthal amplitude variations of the reflections, we plot (Fig. 14a) the synthetic data pertinent to an incidence angle of 15 deg, which is the incident angle we will consider when analysing the actual data, for the entire azimuthal range (0–180 deg). For each azimuthal angle, the strength of the reflection increases as the crack density increases. This increase occurs due to the increase in velocity and density contrasts at the contact between the encasing rock and the fractured zone with increasing crack density.

Another feature that is known to characterize the reflections from an interface separating an overlying isotropic medium from an underlying HTI medium is that the amplitude at a constant incidence angle varies in a sinusoidal fashion with azimuth. By measuring the amplitudes of the reflections at the time corresponding to the fractured zone, we observe such a sinusoidal variation (Fig. 14b), with the minimum amplitude occurring at a 150 deg azimuth (parallel to the fracture strike) and the peak occurring at the orthogonal azimuth of 60 deg. Note that the magnitude of the azimuthal amplitude variation increases with increasing crack density, and the amplitude in the isotropic case (crack density equal to 0) remains constant with azimuth.

We searched for this sinusoidal amplitude behaviour in our observed data, but we encountered several difficulties. The first is the low S/N ratio that characterizes the single bin gathers. In fact, the Larderello–Travale area, with its hard-rock geology, rough topography, accessibility problems and strongly attenuating near surface lithologies, is challenging for reflection seismology (Casini *et al.* 2010). Another drawback is related to the specific acquisition layout that was employed in the survey. As introduced in a previous section, the orthogonal geometry with lines of sources oriented perpendicularly to the lines of receivers yielded an azimuthal coverage that was strongly polarized along the inline direction (Fig. 3), which produced an insufficient azimuthal and offset sampling for each bin gather and even for small ensembles of them. Therefore, we had to resort to averaging the traces of many bin gathers to achieve both fair data quality and sufficient azimuthal distribution for at least some offset ranges. To this end, we examined the offset and azimuth distribution for 300 bin gathers (Fig. 15) located near the well and
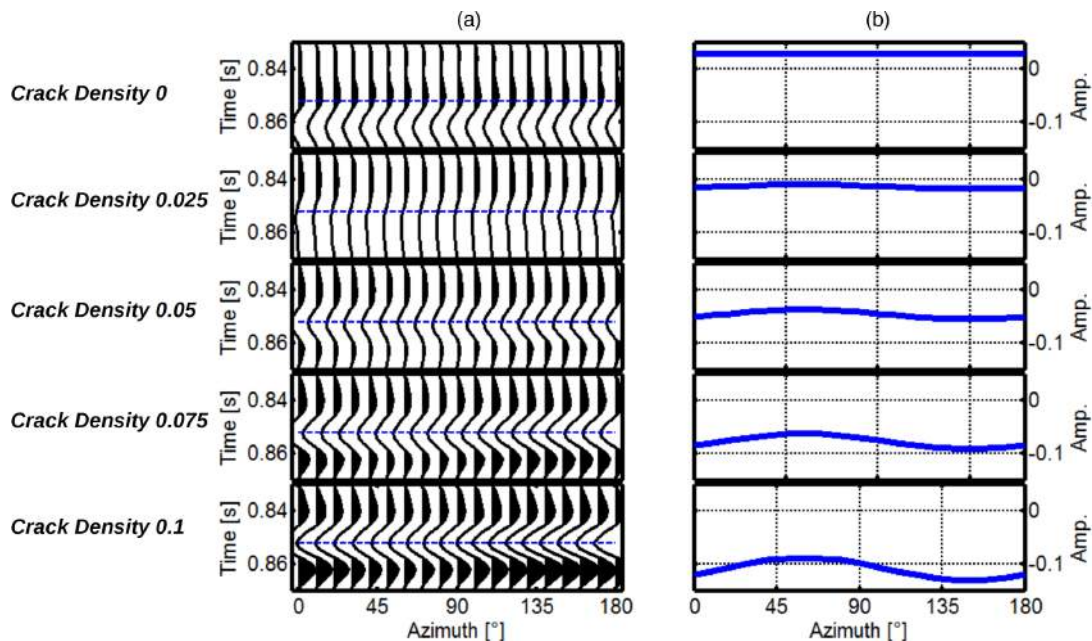

Figure 14. (a) Close-up of the synthetic reflections from the target zone with different crack densities. (b) Amplitude-versus-azimuth variations of the reflections measured along the constant time of the horizontal blue lines in (a). The plotted waveforms in (a) refer to source–receiver azimuths varying from 0 to 180 deg and to a constant incidence angle of 15 deg. The time position of the blue lines in (a) corresponds to the time of the fractured zone.
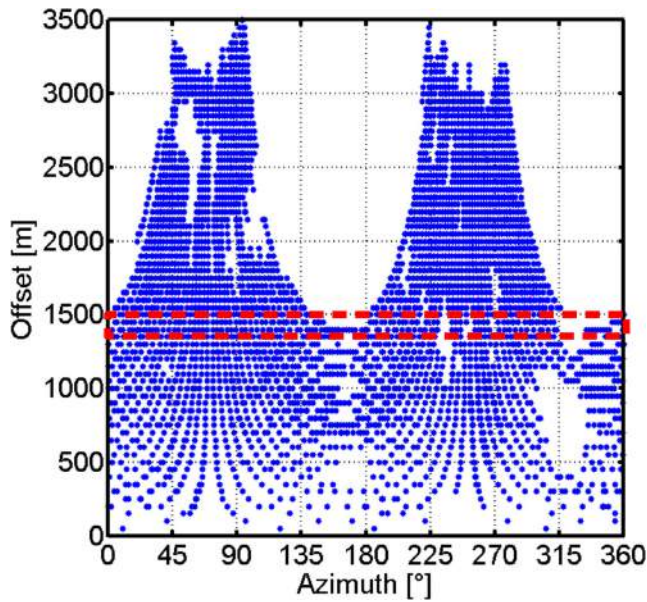
Figure 15. Azimuth-offset distribution for the traces of the bin gathers considered for the azimuthal amplitude analysis. Each dot represents a single trace. The red rectangle contains the traces used in the AVAZ analysis, which pertains to an offset range from 1400 to 1500 m and approximately corresponds to an incidence angle of 15 deg, where a more dense and uniform azimuthal coverage can be found.
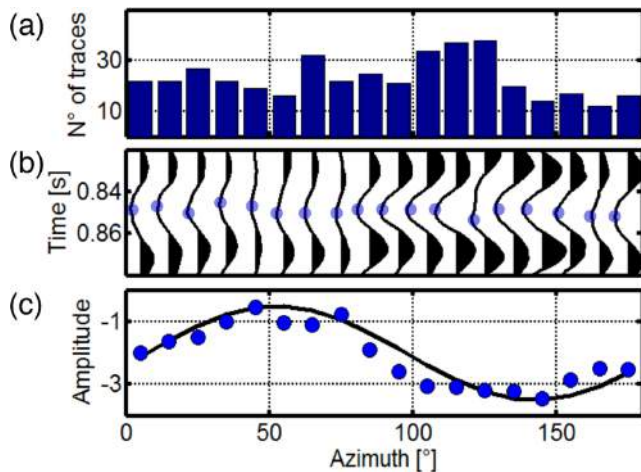

Figure 16. (a) Histogram of the traces to be summed into azimuthal sectors of 10 deg. (b) Close up of the resulting reflections from the fractured level with the blue dots positioned in the troughs. (c) AVAZ response (blue dots) measured at the trough of the reflections and its sinusoidal interpolation.

placed on the aligned features evidenced by the reflection strength and instantaneous phase anomalous lineaments (Figs 7 and 8) that we interpreted as due to fractures. At an offset range from 1400 m to 1500 m, we found a sufficient number of traces with fairly uniform azimuthal coverage and thus we considered this portion of data to analyse the amplitude with azimuth variations. At these source to receiver distances, we estimated an incidence angle of approximately 15 deg. We averaged the traces within azimuthal sectors of 10 deg that have sufficient coverage (Fig. 16a), yielding an azimuth gather of 18 traces (Fig. 16b). A significant amplitude variation with azimuth can be observed in the close-up of the reflections from the fractured level (Fig. 16b). The measured trough amplitudes plotted as a function of azimuth are nicely fitted by a sinusoidal curve that
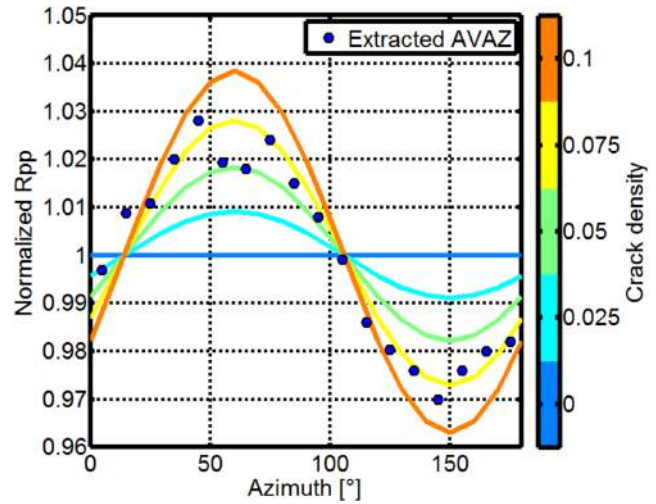

Figure 17. Comparison between the AVAZ responses extracted from the synthetic seismograms computed by considering different crack densities (solid lines) and the AVAZ response extracted from the field seismic data (blue dots). To allow for the comparison of the actual and synthetic AVAZ responses, the amplitudes of each curve have been scaled to a mean of one.

shows a minimum around an azimuth of 140–150 deg (Fig. 16c). As indicated by our modelling experiments, the AVAZ responses of the synthetic data (Fig. 15b) also show the minimum of the sinusoidal amplitude variations at an azimuth of 150 deg, which corresponds to the strike of the fracture planes. Therefore, the results of the AVAZ analysis on the actual data fairly match the synthetic AVAZ responses and the indications given by the CBIL, which evidenced sub-vertical fractures with strikes at approximately 140–160 deg N.

Given that the AVAZ analysis can identify the strike of the fractures in this specific and difficult data case, we now discuss whether it is possible to gain indications on the crack density too. To this end, we compare the actual and synthetic AVAZ curves after proper scaling to mean one (Fig. 17). As previously observed for the comparison between the simulated and recorded elastic properties (Figs 12 and 13), we again find a good match between the synthetic and observed AVAZ responses for a crack density of 0.075.

6 CONCLUSIONS

The deepest geothermal reservoirs in the eastern portion of the Larderello–Travale area are hosted in localized, nearly vertical fractures located near the contact between the Palaeozoic metamorphic basement and the underlying Pliocene granitic intrusion. As shown by well logs, the fractured levels are characterized by densities and seismic velocities lower than those of the surrounding tight rocks. Image logs indicate that the fracture planes within the studied fractured zone have high dips (approximately 80 deg) and are preferentially oriented with a strike direction in the range 140–160 deg N.

Based on bore-hole logs from a deep well, we developed different models to study the effect of fractures on the observed seismic responses in both the post-stack and pre-stack domains. Concerning the post-stack data, we note a good match between the normal incidence synthetic seismogram computed from the *P*-wave velocity and density logs and the actual stack trace that was extracted near the well from the 3-D volume. The strong velocity and density contrasts that occur in correspondence of the fractured zone are the cause of the high-reflection amplitudes that appear in the

synthetic seismogram and in the 3-D seismic data. The 3-D seismic image, particularly the derived attributes of reflection strength and instantaneous phase, constrains the lateral extension of the fractured zone, which manifests itself as an elongated alignment in the NNW-SSE direction with high-reflection strength and as a coincident discontinuity of the instantaneous phase.

To further link the presence of fractures to the velocities and densities observed in the logs and to discuss their effect on the amplitude variations with azimuth (AVAZ) of the reflected signals, we developed several models with different characteristics for the fractured target. In particular, the statistical properties of the logs recorded in the tight intervals and the theoretical derivations by Krasovec *et al.* (1998) and Schoenberg & Sayers (1995) allowed us to simulate different crack densities in the target zone. In all the models, the strike of the fractures was fixed to 150 deg, which is the average strike derived from the CBIL and other image logs. Increasing the crack density progressively reduces the modelled *P*-wave velocity and density and slightly decreases the *S*-wave velocity. A satisfactory match between the modelled and observed properties is found for a crack density of 0.075. For these same models, we computed synthetic seismograms for varying incidence angles and source to receiver azimuths. The AVAZ analysis on the synthetic seismograms shows a sinusoidal trend, with an amplitude minimum that occurs at 150 deg and with an excursion of the sinusoid amplitude that increases with the crack density. The results of the AVAZ analyses performed on the actual data gathers show features that are consistent with the occurrence of fractures with this orientation. However, the irregular azimuthal coverage of the seismic acquisition and the low S/N ratio of the single data gathers forced us to average many common angle—common azimuth traces of many different bin gathers to reach sufficient azimuth coverage and data quality. The elongated features observed in the 3-D seismic volume guided us in the choice of which bin gathers to average. Comparing the amplitude excursion of the synthetic and actual AVAZ sinusoidal trends, we find again a fair match for crack density around 0.075.

Notwithstanding the difficulties of seismic exploration in hard-rock environments and the specific data acquisition and data quality complications found in the study area, the identification and characterization of localized fractured zones by means of reflection seismology, whose effectiveness has been demonstrated for clastic or carbonatic reservoirs, is also feasible for deep metamorphic/intrusive rocks. This feasibility has a specific value for the exploration the Larderello–Travale geothermal area, but it may also be extended to other areas with similar characteristics. Given sufficient data quality and offset and azimuthal coverage, the combined application of rather standard post-stack techniques with AVAZ analysis can provide valuable insights not only for the localization of fractured zones but also for the estimation of the spatial orientation and density of the fractures. However, the applicability of this method depends on several limiting factors, such as the temporal and spatial resolution of the seismic reflection data and the assumption of nearly vertical fractures with common strike. Fractured zones with dimensions below the resolution power and/or characterized by multiple sets of fractures with varying strikes and dips remain challenges for exploration.

ACKNOWLEDGEMENTS

The authors wish to thank ENEL GreenPower for making the seismic and the well log data available and for permission to publish the results. We wish to thank Dr. Marcel Frehner for his constructive criticism and comments and the Editor (Prof. Jörg Renner) for his many suggestions. The seismic data processing was carried out using ProMAX software of Landmark Graphics Corporation, who is gratefully acknowledged.

REFERENCES

Adriansyah & McMechan, G.A., 2001. AVA analysis and interpretation of a carbonate reservoir: northwest Java basin, Indonesia, *Geophysics,* **66**(3), 744–754.

Aki, K. & Richards, P.G., 1980. *Quantitative Seismology: Theory and Methods,* WH Freeman and Co.

Avseth, P., Mukerji, T. & Mavko, G., 2005. *Quantitative Seismic Interpretation: Applying Rock Physics Tools to Reduce Interpretation Risk,* Cambridge University Press.

Backus, G.E., 1962. Long-wave elastic anisotropy produced by horizontal layering, *J. geophys. Res.,* **67**(11), 4427–4440.

Bakku, S.K., Fehler, M. & Burns, D.R., 2012. Fracture characterization from attenuation of Stoneley waves across a fracture, in *Proceedings of the 82nd Annual International Meeting,* SEG, Expanded Abstracts, pp. 1–6.

Baldi, P., Bertini, G., Cameli, G.M., Decandia, F.A., Dini, I., Lazzarotto, A. & Liotta, D., 1994. Tettonica distensiva post-collisionale nell'area geotermica di Larderello (Toscana meridionale), *Stud. Geol. Camerti,* **1,** 183–193.

Barbier, E., 2002. Geothermal energy technology and current status: an overview, *Renew. Sustain. Energy Rev.,* **6**(1), 3–65.

Barelli, A., Cappetti, G. & Stefani, G., 1995. Optimum exploitation strategy at Larderello-Valle secolo, *World Geotherm. Congr.,* **3,** 1779–1783.

Barelli, A., Bertini, G., Buonasorte, G., Cappetti, G. & Fiordelisi, A., 2000. Recent deep exploration results at the margins of the Larderello-Travale geothermal system, *World Geotherm. Congr.,* **2000,** 965–970.

Batini, F., Cameli, G.M., Lazzarotto, A. & Liotta, D., 2003. Line CROP 18: Southern Tuscany, *Mem. Descr. Carta Geol. d'It* **62,** 137–144.

Batzle, M. & Wang, Z., 1992. Seismic properties of pore fluids, *Geophysics,* **57**(11), 1396–1408.

Bertini, G., Cameli, G.M., Costantini, A., Decandia, F.A., Di Filippo, M., Dini, I. & Toro, B., 1991. Struttura geologica fra i monti di Campiglia e Rapolano Terme (Toscana meridionale): stato attuale delle conoscenze e problematiche, *Stud. Geol. Camerti,* **1,** 155–178.

Bertini, G., Casini, M., Ciulli, B., Ciuffi, S. & Fiordelisi, A., 2005. Data revision and upgrading of the structural model of the Travale geothermal field (Italy), in *Proceedings of the 2005 World Geothermal Congress*, pp. 1–4.

Bertini, G., Casini, M., Gianelli, G. & Pandeli, E., 2006. Geological structure of a long-living geothermal system, Larderello, Italy, *TerraNova,* **18**(3), 163–169.

Boccaletti, M., Coli, M., Decandia, F.A., Giannini, E. & Lazzarotto, A., 1980. Evoluzione dell'Appennino settentrionale secondo un nuovo modello strutturale, *Mem. Soc. Geol. Ital.,* **21,** 359–373.

Carmignani, L. & Kligfield, R., 1990. Crustal extension in the Northern Apennines: the transition from compression to extension in the Alpi Apuane core complex, *Tectonics,* **9**(6), 1275–1303.

Carmignani, L., Decandia, F.A., Fantozzi, P.L., Lazzarotto, A., Liotta, D. & Meccheri, M., 1994. Tertiary extensional tectonics in Tuscany (northern Apennines, Italy), *Tectonophysics,* **238**(1), 295–315.

Carmignani, L., Decandia, F.A., Disperati, L., Fantozzi, P.L., Lazzarotto, A., Liotta, D. & Oggiano, G., 1995. Relationships between the Tertiary structural evolution of the Sardinia-Corsica-Provençal Domain and the Northern Apennines, *TerraNova,* **7**(2), 128–137.

Casini, M., Ciuffi, S., Fiordelisi, A., Mazzotti, A. & Stucchi, E., 2010. Results of a 3-D seismic survey at the Travale (Italy) test site, *Geothermics,* **39**(1), 4–12.

Dvorkin, J., Gutierrez, M. & Grana, D., 2014. *Seismic Reflections of Rock Properties,* Cambridge University Press.

Giustiniani, M., Tinivella, U. & Nicolich, R., 2015. Reflection seismic sections across the Geothermal Province of Tuscany from reprocessing CROP profiles, *Geothermics,* **53,** 498–507.

Gray, D., Head, K.J., Chamberlain, C.K., Olson, G., Sinclair, J. & Besler, C., 1999. *Strike Analysis: A Core Matter,* AAPG Explorer, 9.

Jolivet, L., Dubois, R., Fournier, M., Goffé, B., Michard, A. & Jourdan, C., 1990. Ductile extension in alpine Corsica, *Geology,* **18**(10), 1007–1010.

Jolivet, L., Faccenna, C., Goffé, B., Mattei, M., Rossetti, F., Brunet, C. & Parra, T., 1998. Midcrustal shear zones in postorogenic extension: example from the northern Tyrrhenian Sea, *J. Geophys. Res.: Solid Earth* (1978–2012), **103**(B6), 12 123–12 160.

Kent, T., Louie, J. & Echols, J., 2013. Correlating azimuthal anisotropy to geothermal resource potential using a 3D-3C seismic survey of Soda Lake geothermal field, Nevada, in *Proceedings of the 83rd Annual International Meeting,* SEG, Expanded Abstracts, pp. 341–346.

Krasovec, M.L., Rodi, W.L. & Toksoz, M.N., 1998. Sensitivity analysis of amplitude variation with offset (AVO) in fractured media, in *Proceedings of the 68th Annual International Meeting,* SEG, Expanded Abstracts, pp. 201–203.

Lamarche, G., 1992. Seismic reflection survey in the geothermal field of the Rotorua Caldera, New Zealand, *Geothermics,* **21**(1), 109–119.

Lüschen, E., Wolfgramm, M., Fritzer, T., Dussel, M., Thomas, R. & Schulz, R., 2014. 3-D seismic survey explores geothermal targets for reservoir characterization at Unterhaching, Munich, Germany, *Geothermics,* **50,** 167–179.

Lynn, H.B., Simon, K.M. & Bates, C.R., 1996. Correlation between P-wave AVOA and S-wave traveltime anisotropy in a naturally fractured gas reservoir, *Leading Edge,* **15**(8), 931–935.

Mallick, S., Craft, K.L., Meister, L.J. & Chambers, R.E., 1998. Determination of the principal directions of azimuthal anisotropy from P-wave seismic data, *Geophysics,* **63**(2), 692–706.

Matsushima, J., Okubo, Y., Rokugawa, S., Yokota, T., Tanaka, K., Tsuchiya, T. & Narita, N., 2003. Seismic reflector imaging by prestack time migration in the Kakkonda geothermal field, Japan, *Geothermics,* **32**(1), 79–99.

Morland, L.W., 1974. Continuum model of regularly jointed mediums, *J. geophys. Res.,* **79**(2), 357–362.

Nakagome, O., Uchida, T. & Horikoshi, T., 1998. Seismic reflection and VSP in the Kakkonda geothermal field, Japan: fractured reservoir characterization, *Geothermics,* **27**(5), 535–552.

Pussak, M., Bauer, K., Stiller, M. & Bujakowski, W., 2014. Improved 3-D seismic attribute mapping by CRS stacking instead of NMO stacking: application to a geothermal reservoir in the Polish Basin, *J. Appl. Geophys.,* **103,** 186–198.

Robertson, J.D. & Fisher, D.A., 1988. Complex seismic trace attributes, *Leading Edge,* **7**(6), 22–26.

Ruger, A., 1997. P-wave reflection coefficients for transversely isotropic models with vertical and horizontal axis of symmetry, *Geophysics,* **62**(3), 713–722.

Schoenberg, M. & Sayers, C.M., 1995. Seismic anisotropy of fractured rock, *Geophysics,* **60**(1), 204–211.

Shen, F., Sierra, J., Burns, D.R. & Toksöz, M.N., 2002. Azimuthal offset-dependent attributes applied to fracture detection in a carbonate reservoir, *Geophysics,* **67**(2), 355–364.

Taner, M.T., 2001. Seismic attributes, *Can. Soc. Explor. Geophys. Recorder,* **26**(9), 48–56.

Taner, M.T., Koehler, F. & Sheriff, R.E., 1979. Complex seismic trace analysis, *Geophysics,* **44**(6), 1041–1063.

Tang, X.M., Cheng, C.H. & Toksöz, M.N., 1991. Stoneley-wave propagation in a fluid-filled borehole with a vertical fracture, *Geophysics,* **56**(4), 447–460.

Thomsen, L., 1986. Weak elastic anisotropy, *Geophysics,* **51**(10), 1954–1966.

Vetri, L., Loinger, E., Gaiser, J., Grandi, A. & Lynn, H., 2003. 3D/4C Emilio: azimuth processing and anisotropy analysis in a fractured carbonate reservoir, *Leading Edge,* **22**(7), 675–679.

APPENDIX A: BUILDING STEPS OF THE FRACTURED MODELS

The steps to build the fractured models are as follows:

(1) Form a matrix with the *P*-wave, *S*-wave and density values in the tight rock, compute its covariance matrix and make it equal to the covariance matrix of the *P*-wave, *S*-wave and density values in the simulated fractured layer. This enables us to generate velocities and density for any given vertical position in the simulated fractured zone with the same correlation as those in the tight rock.

(2) Compute the autocorrelation of the *P*-wave velocity values (or *S*-wave velocities or densities) in the tight encasing rock and make it equal to the autocorrelation of the simulated properties along the depth segment of the fractured zone. This enables us to generate realistic, vertically coupled velocities and densities (see Dvorkin *et al.* 2014).

(3) From the average *P*-wave and *S*-wave velocities and density computed from the logs in the tight encasing rock, derive the average Lamé parameters of the isotropic rock (i.e. of the target level in its ideal un-fractured status).

(4) Making use of the Batzle and Wang equations (Batzle & Wang 1992), compute the bulk modulus of the saturating fluid filling the simulated fractures. In accordance with the geothermal nature of the reservoir, we assumed vapor as the saturating fluid.

(5) Design models of fractured zones with different crack densities and compute the related elasticity tensor (see Appendix B) following Schoenberg & Sayers (1995) and Krasovec *et al.* (1998). The strike of the fractures and the properties of the encasing isotropic media remain constant for all the models.

(6) From the elasticity tensor, derive the average Thomsen anisotropic parameters and the average *P*-wave and *S*-wave velocities for the HTI fractured zone of each model (see Appendix B). The densities are given by the weighted averages of the isotropic rock's mean density and the density of the fluid that fills the fractured volume.

(7) Assuming Gaussian distributed elastic properties, generate vertically correlated *P* wave, *S* wave and density values for the fractured zone in each model. The average *P*-wave and *S*-wave velocity and density values are equal to the respective means that were computed in the previous step, whereas their covariance at each given vertical position is equal to the covariance of the tight rock properties computed in step 1. The vertical correlation for each elastic property is equal to the autocorrelation computed in step 2. The *S*-wave velocity considered in this paper refers to the propagation along the isotropy plane, that is, a plane parallel to the fracture planes (see Appendix B).

APPENDIX B: MODELLING THE ELASTIC PROPERTIES AND THE AVAZ RESPONSE OF AN HTI MEDIUM

According to Morland (1974), the behaviour of seismic waves traveling through fractured rocks can be described using crack compliances. Crack compliances can be computed with the method described in Schoenberg & Sayers (1995). As reported in Krasovec *et al.* (1998), the Schoenberg's compliances are:

$$E_N = \frac{4e}{3T_b}\left(1 - T_b + \frac{K_f}{\pi\alpha\mu_b}\right)^{-1},$$

$$E_T = \frac{16e}{3(3 - 2T_b)}, \tag{B1}$$

where E_N and E_T are the normal and tangential compliances, respectively. In the above equations, T_b is the squared ratio of the *S*-wave to *P*-wave velocity in the background, μ_b is the shear modulus of the background, α is the fracture aspect ratio, e is the fracture density per volume (crack density) and K_f is the bulk modulus of the saturating fluid. For weak anisotropy (spatial variations in elastic properties due to fractures smaller than the shortest wavelength of interest), the background Lamé constants and the two crack compliances discussed above can be used to describe an effective transversely isotropic medium. According to Schoenberg & Sayers (1995), this medium is equivalent to the fractured rock at the seismic scale. For vertically aligned fractures, the resulting horizontal transverse isotropic (HTI) medium can be completely described by five independent elastic constants:

$$C_{\mathrm{HTI}} = \begin{pmatrix} C_{11} & C_{13} & C_{13} & & & \\ C_{13} & C_{13} & C_{33}-2C_{44} & & & \\ C_{13} & C_{33}-2C_{44} & C_{33} & & & \\ & & & C_{44} & & \\ & & & & C_{55} & \\ & & & & & C_{55} \end{pmatrix},$$

(B2)

The constants in the elasticity tensor (A2) can be computed using the following formulae (Krasovec *et al.* 1998):

$$C_{11} = (\lambda_b + 2\mu_b)/(1 + E_N),$$
$$C_{33} = C_{22} = (\lambda_b + 2\mu_b - \lambda_b^2 E_N)/((\lambda_b + 2\mu_b)(1 + E_N)),$$
$$C_{13} = C_{12} = \lambda_b/(1 + E_N),$$
$$C_{44} = \mu_b/(1 + E_T),$$
$$C_{55} = C_{66} = \mu_b,$$

(B3)

where λ_b is the first Lame's parameter of the background. These elastic constants are used to derive the seismic velocity of waves propagating perpendicular and parallel to the fracture set and to compute the Thomsen (1986) parameters (δ, ε and γ), which are dimensionless combinations of elastic moduli that characterize transversely isotropic materials. In terms of the components of the elastic stiffness matrix, the anisotropic Thomsen parameters are defined as follows:

$$\varepsilon = \frac{C_{11} - C_{33}}{2C_{33}},$$

$$\delta = \frac{(C_{13} + C_{55})^2 - (C_{33} - C_{55})^2}{2C_{33}(C_{33} - C_{55})},$$

$$\gamma = \frac{C_{66} - C_{44}}{2C_{44}},$$

(B4)

The *P*-wave (Vp) and *S*-wave (Vs) velocities are

$$Vp = \sqrt{C_{33}/\rho},$$
$$Vs_{//} = \sqrt{C_{44}/\rho},$$
$$Vs_{\perp} = \sqrt{C_{55}/\rho},$$

(B5)

where ρ denotes density and $Vs_{//}$ and $Vs_{\perp}$ are the isotropy-plane and symmetry-plane shear wave velocities, respectively. We remind that for an HTI medium, the isotropy-plane and symmetry-axis plane are parallel and perpendicular to the fracture planes, respectively.

The reflection coefficient (R_{pp}) for incident and reflected *P* waves from an interface separating an isotropic medium from an HTI medium can be determined using the Ruger (1997) approximation, which is valid in the case of small elastic parameter contrasts at the reflecting interface, small incidence angles (less than 30 deg) and weak anisotropy (δ, ε and $\gamma \ll 1$). The Ruger equation, as reformulated by Avseth *et al.* (2005), is

$$R_{pp}^{\mathrm{HTI}}(\theta, \varphi) \approx R_{pp}^{\mathrm{ISO}}(\theta) + \left(\left(\frac{\Delta\delta}{2} + \left(\frac{2\overline{Vs}}{\overline{Vp}} \right)^2 \Delta\gamma \right) \cos^2(\varphi) \right) \sin^2(\theta)$$

$$+ \left(\left(\frac{\Delta\varepsilon}{2} \right) \cos^4(\varphi) + \left(\frac{\Delta\delta}{2} \right) \cos^2(\varphi) \sin^2(\varphi) \right) \sin^2(\theta) \tan^2(\theta),$$

(B6)

where θ is the average of the incidence and transmission angles across the interface, φ is the azimuth measured from the symmetry-axis plane, $\overline{V_p}$ and $\overline{Vs}$ represent the average seismic velocities across the interface and R_{pp}^{HTI} and R_{pp}^{ISO} are the *P*-wave reflection coefficients for the HTI and isotropic case, respectively. The R_{pp}^{ISO} describes the reflection from the contact between two isotropic media and can be computed with the well-known Aki and Richards equation (Aki & Richards 1980). Note that the *S*-wave velocity considered in (A6) refers to $Vs_{//}$.